Observations on the wavenumber spectrum and evolution of an internal wave attractor

JEROEN HAZEWINKEL[1,2], PIETER VAN BREEVOORT[3], STUART B. DALZIEL[2] AND LEO R. M. MAAS[1,3]

[1]Royal Netherlands Institute for Sea Research, P.O. Box 59, 1790 AB Texel, The Netherlands

[2]Department of Applied Mathematics and Theoretical Physics, University of Cambridge, Wilberforce Road, Cambridge CB3 0WA, UK

[3]Institute for Marine and Atmospheric research Utrecht, University Utrecht, Princetonplein 5, 3584 CC Utrecht, The Netherlands

Reflecting internal gravity waves in a stratified fluid preserve their frequency and thus their angle with the gravitational direction. At boundaries that are neither horizontal nor vertical, this leads to a focusing or defocusing of the waves. Previous theoretical and experimental work has demonstrated how this can lead to internal wave energy being focused onto 'wave attractors' in relatively simple geometries. We present new experimental and theoretical results on the dynamics of wave attractors in a nearly two-dimensional trapezoidal basin. In particular, we demonstrate how a basin-scale mode forced by simple mechanical excitation develops an equilibrium spectrum. We find a balance between focusing of the basin-scale internal wave by reflection from a single sloping boundary and viscous dissipation of the waves with higher wavenumbers. Theoretical predictions using a simple ray-tracing technique are found to agree well with direct experimental observations of the waves. With this we explain the observed behaviour of the wave attractor during the initial development, steady forcing, and the surprising increase of wavenumber during the decay of the wave field after the forcing is terminated.

1. Introduction

Understanding the behaviour of linear internal waves in bounded geometries has relevance to oceanography, astrophysics and fluid dynamics in general. The dispersion relation describing the internal waves, $\omega = N \cos\theta$, relates the frequency ω of the internal waves to the buoyancy frequency N. The wave energy propagates with angle θ with the vertical, with the vertical opposite to the gravitational direction. However, unlike the more familiar surface waves, the dispersion relation does not restrict the wave vector $\boldsymbol{k} = k(\cos\theta, \sin\theta)$ other than being perpendicular to the group velocity (Phillips 1977; LeBlond & Mysak 1978; Maas 2005). The dispersion relation predicts that reflection of the internal waves at boundaries that are neither horizontal nor vertical, leads to a focusing or defocusing of the waves. Maas & Lam (1995) showed that in almost all confined fluid domains wave energy focusing dominates defocusing, leading to a so-called wave attractor. The experimental confirmation of such an attractor in a trapezoidal domain was presented in Maas *et al.* (1997) and re-analysed by Lam & Maas (2008). In this experiment a nearly two-dimensional container, filled with a linearly stratified fluid, was vertically oscillated. Displacement of dye lines was

used to visualize the internal dynamics. Starting from a rest position, an attractor grew due to subharmonic parametric instability. This instability is a linear mechanism that leads to the growth of a perturbation with half the forcing frequency as a result of the modulation of the gravitational acceleration (Benielli & Sommeria 1998). Lam & Maas (2008) revealed that the amplitude of the isopycnal displacements on the attractor had an exponential growth before reaching saturation. Contrary to the growth of a regular mode, the saturation time varied from position to position. They also proposed a causal connection between forcing of a surface seiche and the internal wave field.

Wave attractors are also found for the analogous class of inertial waves supported by homogeneous rotating fluids (Stewartson 1971; Maas 2005). Experimentally, inertial wave attractors have been observed and studied by Maas (2001) and Manders & Maas (2003). They considered a rotating rectangular tank with a sloping wall. From the comparison between the small tank of Maas (2001) and the larger tanks of Manders & Maas (2003), it appears that the width of the attractor branches is independent of viscosity. This led Manders & Maas (2004) to the conclusion that the spatial scale of the observed attractors is set by nonlinear processes. However, in the theoretical work by Rieutord, Valdettaro & Georgeot (2001, 2002) viscous processes were assumed to set the scale. Also, Ogilvie (2005) considered the low-viscosity limit and provided a way of calculating the dissipation rate. In these models the dissipative spreading of the waves balances the geometric focusing due to reflections.

The purpose of this paper is to contribute to the above discussion of what sets the attractor scale. In this context, we define the scale of the attractor as the dominant wavelength, perpendicular to the attractor branches, corresponding to the peak in the wavenumber spectrum (to be discussed later). We have conducted experiments and present the observed data mainly as spectra of the wavenumber k. We show that a balance exists between amplification by focusing at the sloping wall and dissipation at the highest wavenumbers.

2. Method

For the experiment we use a narrow rectangular tank with one sloping endwall at an angle of $27°$ to the vertical (see figure 1). Although the tank has finite width, we refer to it as nearly two-dimensional. This is because the symmetry is broken by the slope so the wave motion will primarily depend on the along-tank and vertical coordinates, x and z respectively, and will be essentially uniform in the narrow, cross-tank (y) direction. (See table 1 for the dimensions of the tank.) The tank is filled with a stratification comprising a layer of depth $H = 190 \pm 2$ mm, in which the density decreases linearly upwards, beneath a shallow mixed surface layer. The presence of this mixed layer does not affect the dynamics of the stratified layer and so we shall exclude it from our discussion. Filling the tank with the well-known double-bucket technique is not possible as the domain has a cross-section that varies with height. Instead, we use two computer-controlled Masterflex peristaltic pumps that enable us to fill the tank with any desired stratification. We present the findings of experiments performed in a fluid with constant buoyancy frequency $N = \sqrt{-g/\rho_0 \, \mathrm{d}\bar{\rho}(z)/\mathrm{d}z} = 3 \pm 0.1 \, \mathrm{rad\,s^{-1}}$, where ρ_0 is a reference density. Here, we measure the background stratification $\bar{\rho}(z)$ by taking 10 density samples. Although our choice of N pushes the limit of the Boussinesq approximation, using smaller values of N is found to make no difference other than that it affects the quality of the visualization.

Forcing period	T	5.1	s
Buoyancy frequency	N	3	rad s^{-1}
Fluid height	H	190	mm
Dimensions of tank	$h \times w \times L_{bot}$	$330 \times 101 \times 453$	mm
Angle of sloping wall	α	0.47	rad
Forcing frequency	ω_e	$2\pi/T = 1.23$	rad s^{-1}
Forcing amplitude	A_e	120	mm
Duration forced stage		$50 \times T = 255$	s
Duration decay stage		$40 \times T = 204$	s

TABLE 1. Parameter values of the experiment, described in §2.

To measure the motions in the fluid non-intrusively, we use the synthetic schlieren technique (Dalziel, Hughes & Sutherland 2000). Synthetic schlieren measures the refractive index changes of a medium resulting from density perturbations. The principle is as follows. When a light-ray propagates through the fluid, the direction of propagation of this ray will be altered by the local value of the gradient of the index of refraction. A random dot pattern on a light bank 0.5 m behind the tank and fixed in the laboratory frame is monitored through the fluid. Density perturbations alter the refractive index and hence the direction of the light and are observed as apparent movement of the dots. Unfortunately, the refractive index of the air, between the tank and the point of observation, is also altered by unavoidable temperature fluctuations in the laboratory. This leads to some 'thermal noise' contaminating the observations. To record the apparent movements of the dots, we use a Jai CV-M4+CL camera (1.3 MPixel monochrome) positioned 8 m from the tank. Using an unperturbed reference image, the perturbed position of the dots is translated into corresponding density gradient variations. For this comparison and data processing we use the DigiFlow software. As we observe the changes in the density gradient field, the stronger the undisturbed gradient field is, the more the dots appear to move. Consequently we present results of experiments with large N. We will present the observations as components of $\boldsymbol{b} = (b_x, b_z) \equiv \nabla \rho'/(\mathrm{d}\bar{\rho}/\mathrm{d}z)$, i.e. the perturbation density gradient relative to the gradient of the unperturbed background stratification, $(\mathrm{d}\bar{\rho}/\mathrm{d}z)$.

Initially, we focused on internal wave generation by subharmonic parametric instability. This sort of forcing resulted in the attractor reported by Maas *et al.* (1997) and Lam & Maas (2008). To excite the instability, we use a vertically oscillating platform that carries the tank. However, with forcing amplitude A_e well below the theoretically predicted threshold of the parametric instability, another generation mechanism is already very effective. Owing to slight horizontal movements accompanying the much stronger vertical motion, the stratified fluid in the tank starts sloshing a little, with an estimated amplitude of 0.5 mm. This barotropic motion is strong enough to generate baroclinic internal waves from its interaction with the slope. (Installing a rigid lid on the surface prevented this sloshing and effectively removed any measurable internal wave generation.) The generated internal waves have a frequency ω equal to that of the excitation, i.e. $\omega = \omega_e$. The results presented in this paper are for internal waves that are generated by this barotropic motion of the fluid.

The experiment is performed as follows. After 1 period, $T = 2\pi/\omega_e$, of linearly increasing the amplitude to A_e, the platform is vertically oscillated with frequency ω_e for $49T$. During this stage the camera is triggered to capture images at three fixed
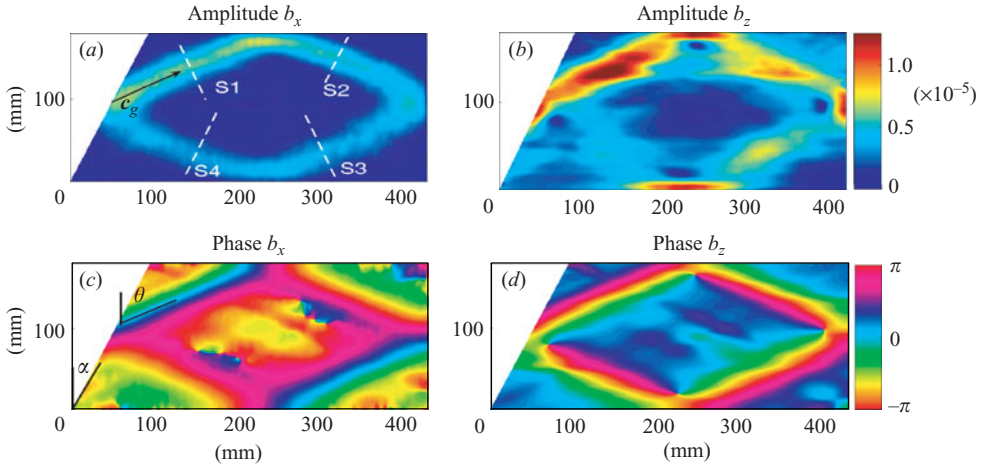
FIGURE 1. Harmonic analysis of the observations of b_x (left) and b_z (right). (a, b) The amplitude. The black arrow in (a) gives the direction of the group velocity $\boldsymbol{c}_g$ pointing in the direction of energy propagation. The white lines indicate sections S1–S4, perpendicular to the corresponding four branches of the attractor. The phase is shown in (c, d). Slope angle α and propagation angle θ are indicated in (c).

positions at each cycle of the oscillation. At $t = 50T$ the motion of the platform is linearly damped over two periods. Directly after the platform is at rest, from $t = 52T$ on, the camera captures 24 frames s^{-1} (fps) of the decay stage, over 40 periods.

3. Results

We observe an internal wave attractor with the parameters given in table 1. We present the result of harmonic analysis at frequency $\omega = \omega_e$ of b_x and b_z using the very accurate time series (24 fps) between $t = 52T$ and $t = 54T$. The sloshing of the free surface does not show up in harmonic analysis. The amplitudes are shown in figure 1(a, b); the figures have been cropped to the boundaries of the tank and to the bottom of the mixed surface layer. The orthogonal sections over the four attractor branches, represented by the white dashed lines in figure 1(a), are for later use and will be referred to as S1–S4. The corresponding phases of the internal wave fields are shown in figure 1(c, d). The angles of the sloping wall, α, and of the internal waves, θ, are indicated in figure 1(c). Note that the phase of b_x is inverted upon each reflection, while that of b_z is maintained.

The spatial structure of the perturbation and phase take the form of an internal wave attractor, as originally observed by Maas *et al.* (1997). The sloping wall focuses waves propagating in a clockwise sense. The phase propagation is perpendicular to the attractor branches, indicating that the group velocity, and thus the energy, propagates clockwise, as indicated by the black arrow. Following the energy from the sloping wall along the attractor, it is clear that the intensity of the density perturbation decreases, reaching a minimum just before the sloping wall. Also, the intensification at the reflection points is observed, being the result of (linear) superposition of the incident and reflected branches.

After starting the oscillating platform, the attractor grows from the initial undisturbed state. The growth of b_z in the middle of S1 is shown in figure 2. There is clearly an initial growth stage reaching an equilibrium after $t = 25T$. Throughout
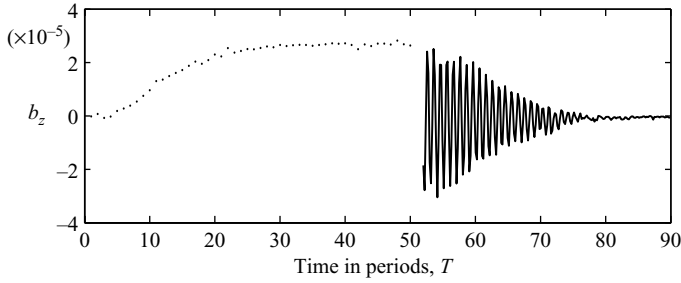
FIGURE 2. Observed growth and decay of b_z in the middle of S1. Note that the observation in the forced stage is once per period while the decay is shown in much more detail (125 obs/T).
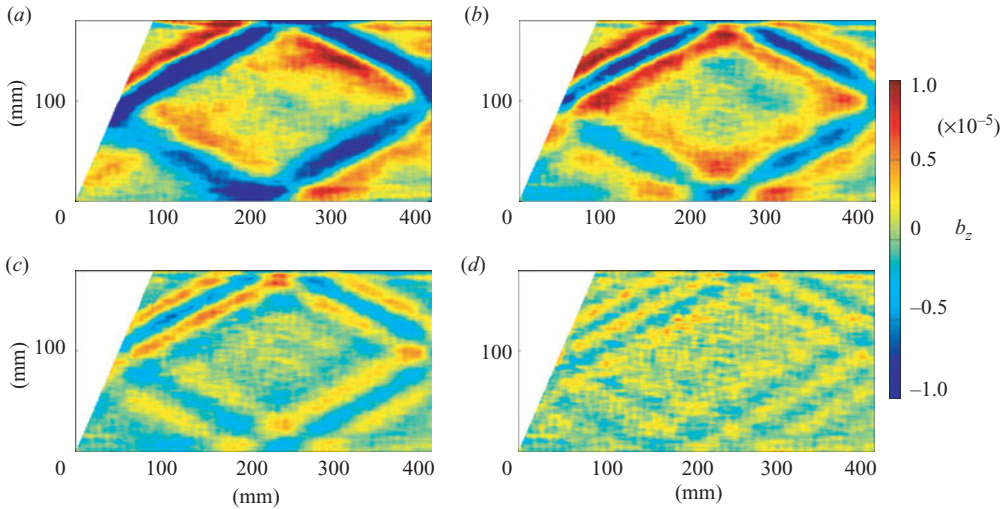

FIGURE 3. Four snapshots of b_z, at (*a*) $t = 52T$ (beginning of decay stage), (*b*) $t = 60T$, (*c*) $t = 68T$ and (*d*) $t = 76T$, showing that the shorter wavelengths decay later.

the decay stage ($t > 52T$) the frequency of the attractor remains well preserved with $\omega = \omega_e \pm 0.05 \, \text{rad s}^{-1}$. The dispersion relation therefore ensures that θ is preserved, as can be seen in figure 3 where four snapshots of the decay stage are presented. Rather surprisingly, these snapshots suggest that the wavelength of the attractor decreases. This seem contrary to the notion that diffusive processes eliminate the short wavelengths. The snapshots confirm that the magnitude of the perturbation decays everywhere in the tank, similar to the observation in figure 2.

3.1. *Spectral analysis*

The remarkable presence of several wavelengths during the decay suggests that there is value in analysing the wavenumber spectrum. We introduce a coordinate system that aligns with the branches and the wave vector $\boldsymbol{k} = k(\cos\theta, \sin\theta)$ in the (x, z)-plane. In particular, η is the coordinate along section S1, increasing from top left to bottom right, and is given by $\eta = x\cos\theta - z\sin\theta$. The buoyancy gradient in the direction of η is $b_\eta = b_x \cos\theta - b_z \sin\theta$, and we assume that this can be written as

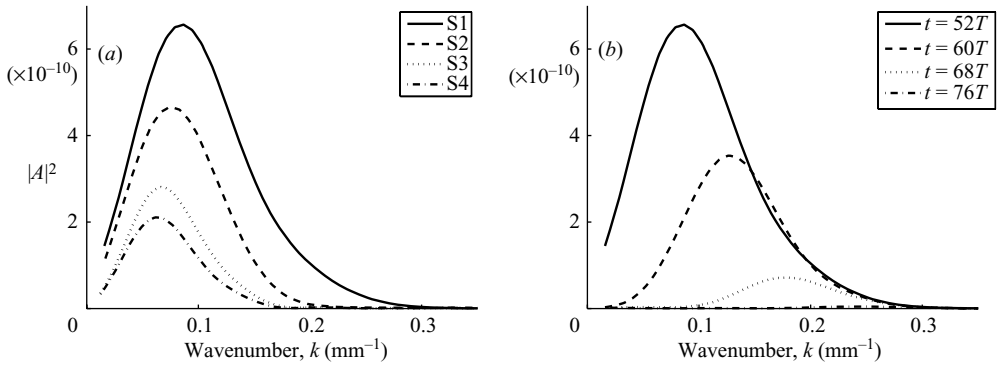$$b_\eta = \int A(k)e^{i(k\eta - \omega t)} \, dk. \tag{3.1}$$

FIGURE 4. (*a*) Viscous broadening from S1 to S4 at $t = 52T$. (*b*) Time evolution of the spectrum along S1 at $t = 52T$, $60T$, $68T$ and $70T$.

Note that η is redefined along S2–S4. Ideally, the complex amplitudes $A(k)$ are obtained by Fourier transform of b_η, where the amplitude fields of harmonic analysis are used to construct b_η (fields such as in figure 1). However, harmonic analysis is only possible in the decay stage as the few observations in the forced stage, i.e. three per cycle, prove to be insufficient to adequately reproduce the amplitudes. Instead, for $t < 50T$, we must approximate $A(k)$ using a Fourier transform of the b_η field from the instantaneous gradient fields. Examining this approximation for $t \geqslant 52T$ shows that it reproduces the main qualitative features of the full spectrum. As is standard when performing Fourier analysis on non-periodic signals, we add to every section a sequence of zeros, so-called zero-padding. This allows us to plot nearly continuous spectral lines (and contour plots) in figures 4–6.

The spectra of S1–S4 from harmonic analysis, over the first period of the decay, are presented in figure 4(*a*). Comparing the spectra, we see a clear shift of the spectral peak towards low wavenumbers as we move from S1 to S4. This can also be seen in figure 3(*a*), at $t = 52T$, with a broadening of the branches on going from S1 and S4. From the spectra we learn that, on following their path around the attractor, the high wavenumbers disappear and the low wavenumbers remain. This viscous broadening of the attractor branches corresponds to the decrease in dominant wavenumber.

However, as the attractor decays we observe that the low wavenumbers (large wavelengths) disappear. The spectra for S1 from harmonic analysis around the same moments during the decay as in figure 3 are shown in figure 4(*b*). Apart from a decrease of total amplitude, we indeed see a clear shift of the peak towards the high wavenumbers

Approximate spectra for S1 from instantaneous fields during growth, equilibrium and decay stages are combined in figure 5. It shows in false colour the 'energy' $|A(k)|^2$ (i.e. the square of the spectral amplitude of the buoyancy gradient) as a function of wavenumber (horizontal axis) and time (vertical axis). At the start of the experiment, $t = 0$, there are no waves. The spectrum grows from the lowest wavenumbers towards the high wavenumbers. Thermal fluctuations in the laboratory contaminate the spectra, most notably at $t = 22T$ and $t = 42T$. By $t = 25T$ the spectrum reaches equilibrium, coinciding with the saturation of the amplitude of the density gradient perturbation in figure 2. After the oscillation of the platform is stopped, $t > 52T$, we observe the decay of the spectrum. It is clear that, as time passes, the energy at low k values decays fastest, while that at high wavenumbers persists. This is in accordance with the qualitative observation of the structure in figure 3. Note that

high-wavenumber energy exists from the time the spectrum reaches equilibrium onwards. However, the energy at high wavenumbers is overshadowed by that of the stronger low wavenumbers until the forcing is halted. Only when the high wavenumbers become dominant do they determine the scale of the attractor branch.

4. Simple model

In this section we present a model explaining the observed characteristics of the wavenumber spectrum in the growth and decay stage. Subsequently, the equilibrium spectrum will be addressed.

During the growth and equilibrium stages of the experiment the largest waves are driven by sloshing of the fluid in the tank. Propagation of the waves inevitably leads to reflection at the walls. Every time these waves reflect at the sloping wall in a clockwise (focusing) sense, their wavenumber increases (wavelength decreases) by a factor

$$\gamma = \frac{\sin(\theta + \alpha)}{\sin(\theta - \alpha)}. \tag{4.1}$$

For the parameters given in table 1 this yields focusing power $\gamma \approx 1.6$. The amplitude of the wave is amplified by the same ratio, as conservation laws demand. This results in a continuous transfer of energy towards the high wavenumbers. This transfer is also dependent on group speed $c_g(k) = |\boldsymbol{c}_g| = N \sin\theta/k$, which decreases with increasing k. We define the different loop times, the time needed for the energy in wavenumber k to travel once around the attractor of length L_a:

$$t_{loop}(k) = \frac{L_a}{c_g(k)} = \frac{L_a k}{N \sin\theta}. \tag{4.2}$$

We also define a sequence of focused wavenumbers

$$k_n = \gamma k_{n-1} = \gamma^n k_0, \tag{4.3}$$

with $k_0 = 2\pi/H$, the wavenumber corresponding to the scale of the basin, and n the number of loops around the attractor. Combining (4.2) and (4.3) we define

$$t_{sum}(k_n) = \sum_{i=0}^{n-1} t_{loop}(k_i) = \sum_{i=0}^{n-1} \frac{L_a \gamma^i k_0}{N \sin\theta} = \frac{L_a k_0}{N \sin\theta} \frac{\gamma^n - 1}{\gamma - 1}. \tag{4.4}$$

This is the time passed since the wave had wavenumber k_0. The increase in wavenumber and amplitude is not unlimited. Viscosity acts on the waves and becomes more efficient at dissipating energy at high wavenumbers. This process is the sink for the energy put into the system. A balance between generation/amplification and dissipation is reached in the equilibrium stage; this is addressed in the next section. When we stop the oscillation, and thus the energy input, the transfer of energy towards high k continues. The source for the lowest wavenumber (k_0) however, is now gone.

This ongoing transfer from low to high wavenumbers is seen in figure 5. Here, we see that in the decay stage, the energy associated with the high values of k is sustained much longer at the equilibrium level than is the case at the low wavenumbers. The dashed white lines in figure 5 represent t_{sum}, with $L_a = 850$ mm, starting from arbitrary times. We can see that these lines align with the peak shift in the spectrum in both the growth and decay stage.
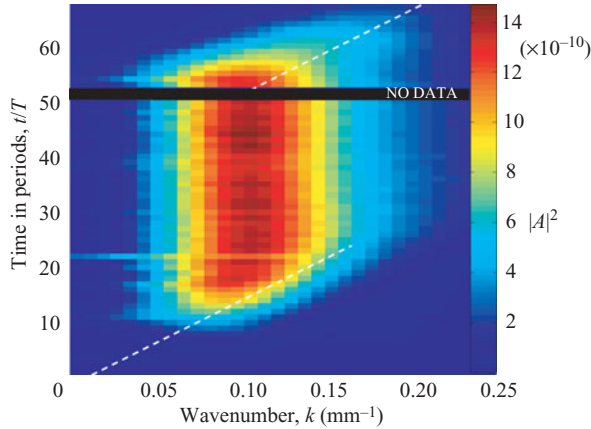
FIGURE 5. Evolution of the wavenumber spectrum along section S1 during the whole experiment. The dashed white lines indicate t_{sum}. The black band ($50 \leqslant t/T \leqslant 52$) indicates the transition from the forced stage to the decay stage.

4.1. *Simple model equilibrium spectrum*

We now address the observed equilibrium spectrum. A balance is assumed between amplification of the amplitude through reflection off the slope and dissipation at the high wavenumbers. Rieutord *et al.* (2001) considered a travelling wave packet along an attractor and described its damping by viscosity as

$$A(k) = A_0 e^{-\nu k^2 t}. \tag{4.5}$$

This follows by inserting (3.1) into a diffusion equation $\partial b_\eta/\partial t = \nu \partial^2 b_\eta/\partial \eta^2$. The viscous damping is of influence over multiple wave periods, $t \gg T$, and we will model damping between successive reflections from the slope for a given packet discretely. We do this by sampling (4.5) at each loop around the attractor. At the sloping wall the wave (k_{n-1}) is focused into a wave with higher wavenumber k_n. Upon reflection the energy flux is preserved, i.e. $F = c_g U^2/2$ is constant, where the particle motion U scales with the perturbation density (Phillips 1977). However, since A refers to the amplitude of the perturbation density gradient, then $U \propto A/k$ implying $A^2 k^{-3}$ is preserved. From this we find the recursive relation $A(k_n)^2 \equiv A_n^2 = \gamma^3 A_{n-1}^2$. Combining this description of focusing with that of the dissipation in (4.5) and the time for each loop, (4.2), then leads to

$$A_n^2 = \gamma^3 \exp\left[\frac{-2\nu L_a k_n^3}{N \sin\theta}\right] A_{n-1}^2 = \gamma^{3n} \exp\left[-\Upsilon(\gamma^{3n} - 1)\right] A_0^2, \tag{4.6}$$

with $\Upsilon = [2\nu/(H^2 N)][L_a/H][(2\pi)^3/((\gamma^3 - 1)\sin\theta)]$. We calculate subsequent wave numbers, starting from k_0 and using appropriate values for our experiment ($\nu = 1 \text{ mm}^2 \text{ s}^{-1}$ and $\omega = 1.23 \text{ rad s}^{-1}$). We find that in eight focusing reflections the largest wavelength is transformed into the smallest wavelength found in our observed spectrum. In figure 6 we plot the observed equilibrium spectrum along S1 (solid line) and our computed A_n^2 from (4.6) (squares). The dashed line indicates the spectrum (4.6) where n is treated as a continuous variable. It is clear that for the lowest wavenumbers the amplification by focusing is dominant (left side of the spectrum $\propto \gamma^{3n}$) and that dissipation mainly acts on the high wavenumbers (right side of the spectrum $\propto \exp[-\Upsilon(\gamma^{3n} - 1)]$). The observed and modelled spectra have
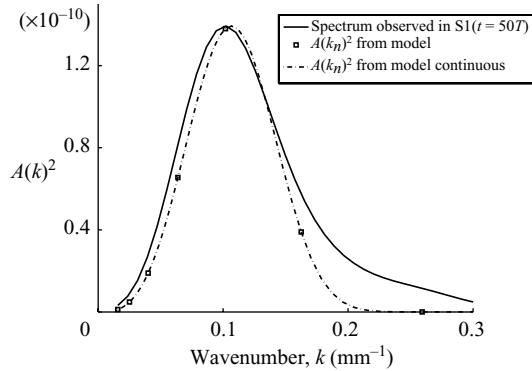
$(\times 10^{-10})$

1.2

0.8

$A(k)^2$

0.4

Spectrum observed in S1$(t = 50T)$
□ $A(k_n)^2$ from model
- · - $A(k_n)^2$ from model continuous

0   0.1   0.2   0.3

Wavenumber, k (mm^{-1})

FIGURE 6. Comparison of the observed equilibrium spectrum and A_n^2 from (4.6).

similar behaviour and indeed show that our assumption of a balance between focusing and viscous dissipation is reasonable. We argue that the difference between observation and model on the dissipation side of the spectrum is caused by noise. Note that (4.6) fixes the structure of the spectrum but not its scale. The amplitude A_0 remains arbitrary and we have matched it to that of our experimental spectrum. While we do not know the actual A_0 for our experiments, we expect that the amplitude of the forcing will play a dominant role in determining A_0 and hence the maximum value of $A(k)$.

5. Discussion and conclusion

From this work it is clear that the observed structure of internal wave attractors can be explained through the linear processes of focusing and viscous diffusion. Focusing takes the energy from the relatively large basin scale, that is most strongly excited by the forcing, to smaller scales where viscous dissipation dominates, overwhelming any further focusing. In these experiments the internal waves at the basin scale were undoubtedly linear. Whilst the wave amplitude increased as the wavelength decreased during the first few cycles of the attractor, this was not sufficient to generate any strong nonlinearities.

In their laboratory experiments, Manders & Maas (2004) observed that the attractor scaled with the tank size. From this they concluded that the scale of the attractor is independent of viscosity. Paradoxically, in the astrophysical context, Rieutord *et al.* (2001) and Ogilvie (2005) found that the scale of the attractor depends on viscosity. We find that the scale of the attractor is set by the spectral peak at wavenumber $k_{peak} = \gamma^{n_{peak}} k_0$. Neglecting the discrete nature of n, the value of n_{peak} is obtained when the derivative of (4.6) with respect to n vanishes, giving $n_{peak} = -\ln(\Upsilon^{1/3})/\ln(\gamma)$. Recalling that $k_0 \propto H^{-1}$, assuming that $L_a \propto H$ and using the relation $p^{\ln q/\ln p} = q$, shows that the length scale of the attractor is $k_{peak}^{-1} \propto (H\nu/N)^{1/3}$. The value of k_{peak} turns out to be strongly dependent on fluid height H when the laboratory range is considered ($200 < H < 1000$ mm, Manders & Maas 2004). However, this does not mean that k_{peak} is independent of the viscosity in this geometry regime. Even at astrophysical scales, the balance between geometry, viscosity and stratification will set the scale of the attractor.

REFERENCES

BENIELLI, D. & SOMMERIA, J. 1998 Excitation and breaking of internal gravity waves by parametric instability. *J. Fluid Mech.* **374**, 117–144.

DALZIEL, S. B., HUGHES, G. O. & SUTHERLAND, B. R. 2000 Whole field density measurements by 'synthetic schlieren'. *Exps. Fluids* **28**, 322–335.

LAM, F.-P. A. & MAAS, L. R. M. 2008 Internal wave focusing revisited; a reanalysis and new theoretical links. *Fluid Dyn. Res.* **40**, 95–122.

LEBLOND, P. H. & MYSAK, L. A. 1978 *Waves in the Ocean*. Elsevier.

MAAS, L. R. M. 2001 Wave focussing and ensuing mean flow due to symmetry breaking in rotating fluids. *J. Fluid Mech.* **437**, 13–28.

MAAS, L. R. M. 2005 Wave attractors: linear yet nonlinear. *Intl J. Bifurcation Chaos* **15**, 2757–2782.

MAAS, L. R. M., BENIELLI, D., SOMMERIA, J. & LAM, F.-P. A. 1997 Observation of an internal wave attractor in a confined stably-stratified fluid. *Nature* **388**, 557–561.

MAAS, L. R. M. & LAM, F.-P. A. 1995 Geometric focusing of internal waves. *J. Fluid Mech.* **300**, 1–41.

MANDERS, A. M. M. & MAAS, L. R. M. 2003 Observations of inertial waves in a rectangular basin with one sloping boundary. *J. Fluid Mech.* **493**, 59–88.

MANDERS, A. M. M. & MAAS, L. R. M. 2004 On the three-dimensional structure of the inertial wave field in a rectangular basin with one sloping boundary. *Fluid Dyn. Res.* **35**, 1–21.

OGILVIE, G. I. 2005 Wave attractors and the asymptotic dissipation rate of tidal disturbances. *J. Fluid Mech.* **543**, 19–44.

PHILLIPS, O. M. 1977 *The Dynamics of the Upper Ocean*, 2nd edn. Cambridge University Press.

RIEUTORD, M., VALDETTARO, L. & GEORGEOT, B. 2001 Inertial waves in a rotating spherical shell: attractors and asymptotic spectrum. *J. Fluid Mech.* **435**, 103–144.

RIEUTORD, M., VALDETTARO, L. & GEORGEOT, B. 2002 Analysis of singular inertial modes in a spherical shell: the slender toroidal shell model. *J. Fluid Mech.* **463**, 345–360.

STEWARTSON, K. 1971 On trapped oscillations of a rotating fluid in a thin spherical shell. *Tellus* **XXII (6)**, 506–510.